ADVANCED ENERGY MATERIALS

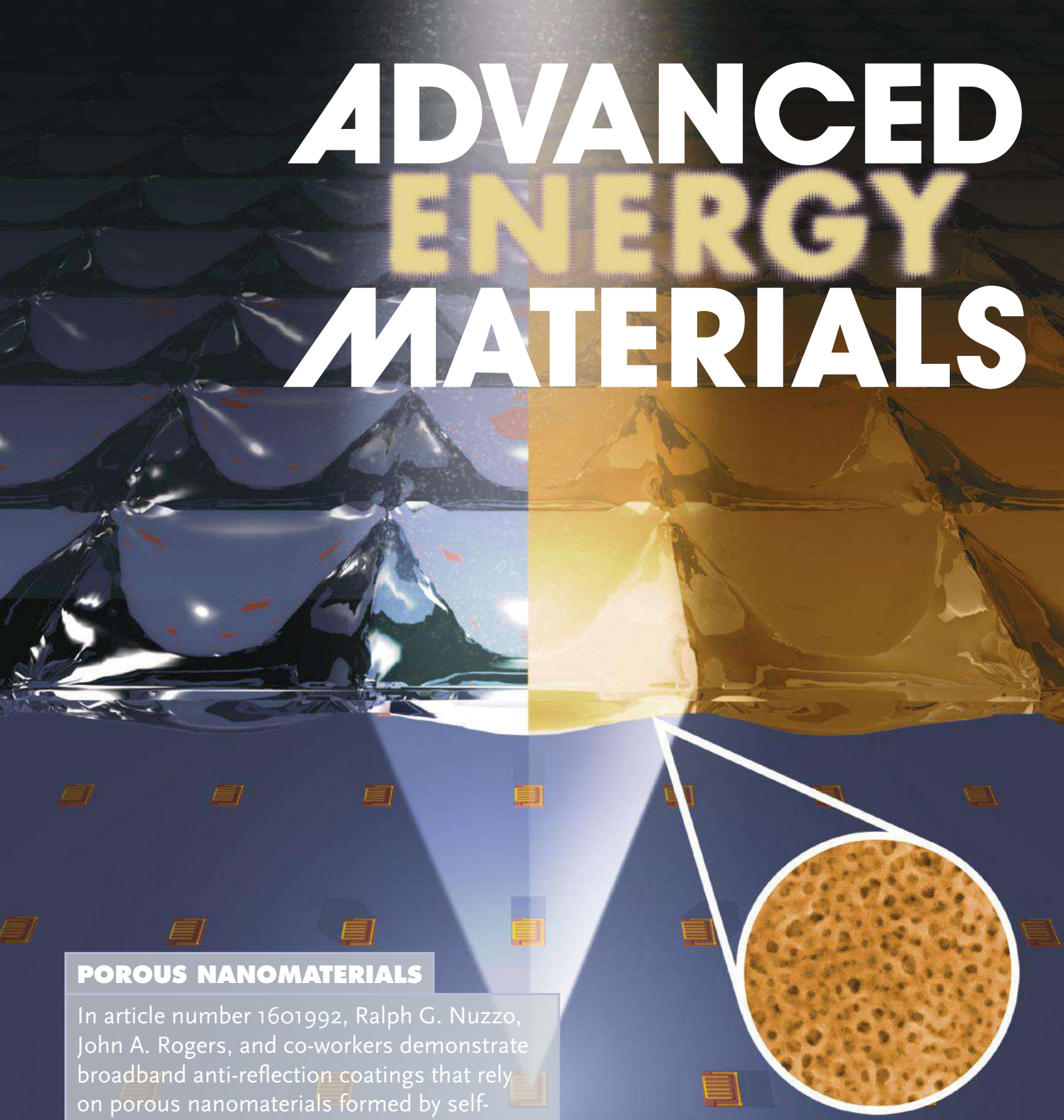

POROUS NANOMATERIALS

In article number 1601992, Ralph G. Nuzzo, John A. Rogers, and co-workers demonstrate broadband anti-reflection coatings that rely on porous nanomaterials formed by self-assembly. The image shows the use of such coatings (orange) on an array of lenses within a concentration photovoltaics architecture, where photons are efficiently concentrated onto underlying triple-junction solar cells, leading to an efficiency enhancement of ≈8%.

WILEY-VCH

Porous Nanomaterials for Ultrabroadband Omnidirectional Anti-Reflection Surfaces with Applications in High Concentration Photovoltaics

Yuan Yao, Kyu-Tae Lee, Xing Sheng, Nicolas A. Batara, Nina Hong, Junwen He, Lu Xu, Muhammad M. Hussain, Harry A. Atwater, Nathan S. Lewis, Ralph G. Nuzzo, and John A. Rogers**

Materials for nanoporous coatings that exploit optimized chemistries and self-assembly processes offer capabilities to reach ≈98% transmission efficiency and negligible scattering losses over the broad wavelength range of the solar spectrum from 350 nm to 1.5 μm, on both flat and curved glass substrates. These nanomaterial anti-reflection coatings also offer wide acceptance angles, up to ±40°, for both s- and p-polarization states of incident light. Carefully controlled bilayer films have allowed for the fabrication of dual-sided, gradient index profiles on plano-convex lens elements. In concentration photovoltaics platforms, the resultant enhancements in the photovoltaics efficiencies are ≈8%, as defined by experimental measurements on systems that use microscale triple-junction solar cells. These materials and their applications in technologies that require control over interface reflections have the potential for broad utility in imaging systems, photolithography, light-emitting diodes, and display technologies.

1. Introduction

Recent advances have made concentration photovoltaics (CPV) technology increasingly attractive for utility scale power generation. Advanced systems incorporate multi-junction (MJ) solar cells that operate on separate spectral bands of solar radiation to reduce carrier thermalization losses, in which the addition of junctions provides a scalable pathway for increasing the photovoltaic (PV) conversion efficiencies.[1] Geometric optical elements that concentrate rays of direct sunlight onto these MJ cells enhance the materials utilization such that in geographic regions with high direct normal irradiance, the cost of electricity generated

Y. Yao, J. He, L. Xu, Prof. R. G. Nuzzo
Department of Chemistry
University of Illinois at Urbana-Champaign
Urbana, IL 61801, USA
E-mail: r-nuzzo@illinois.edu
Dr. K.-T. Lee, Prof. R. G. Nuzzo, Prof. J. A. Rogers
Department of Materials Science and Engineering
Frederick Seitz Materials Research Laboratory
University of Illinois at Urbana-Champaign
Urbana, IL 61801, USA
E-mail: jrogers@illinois.edu
Prof. X. Sheng
Department of Electronic Engineering
Tsinghua University
Beijing 100084, China
N. A. Batara, Prof. H. A. Atwater
Division of Engineering and Applied Sciences
California Institute of Technology
Pasadena, CA 91125, USA
Dr. N. Hong
J. A. Woollam Co., Inc
Lincoln, NE 68508, USA
Prof. M. M. Hussain
Integrated Nanotechnology Lab
CEMSE Division
King Abdullah University of Science and Technology (KAUST)
Thuwal 23955, Saudi Arabia
Prof. H. A. Atwater
The Joint Center for Artificial Photosynthesis
California Institute of Technology
Pasadena, CA 91125, USA
Prof. H. A. Atwater, Prof. N. S. Lewis
Kavli Nanoscience Institute
California Institute of Technology
Pasadena, CA 91125, USA
Prof. N. S. Lewis
Division of Chemistry and Chemical Engineering
Beckman Institute
California Institute of Technology
Pasadena, CA 91125, USA

DOI: 10.1002/aenm.201601992

by the latest CPV modules can compete with conventional flat-plate PV technologies. Many advances in CPV systems follow from the development of epitaxial growth techniques and/or from novel stacking, bonding, and mechanical assembly strategies[2–15] to increase the number of junctions in MJ cells. Over the last decade, cell efficiencies have improved at a rate of roughly 1% per year, to values that are presently ≈46.0%, with corresponding module efficiencies of 38.9%.[16] Alternative approaches that use spectrum-splitting techniques and arrays of separate, single-junction cells are also possible.[17,18] Hybrid optical designs at the module level allow utilization of both direct and diffuse solar radiation, thereby further improving the module level efficiencies.[19–22]

In all of these embodiments, Fresnel reflections associated with the concentrating and/or spectrum splitting optics result in optical losses and, by consequence, reductions in performance. For the most advanced commercial CPV modules (Semprius Inc.) in a two-stage optics system (i.e., a primary lens array along with ball lenses, the latter of which enhance the angular acceptance and illumination uniformity), such losses are ≈12% due to the presence of three optic/air interfaces.[23] Although reflections at the surfaces of MJ cells can be minimized using standard multilayer coating approaches, reflections at the air/glass interfaces are much more difficult to address technically. The simplest approach relies on a single-layer coating having an index of refraction intermediate between the air and the substrate (i.e., $n_{opt} = \sqrt{n_i \cdot n_s}$ where n_i and n_s are the refractive indices of the incident medium and the substrate, respectively) optimized for operation at a given wavelength by selecting a thickness equal to a quarter of the wavelength evaluated in the coating (i.e., $t = \lambda/4n_{opt}$). Multilayer coatings increase the wavelength bandwidth for effective operation, as demonstrated on a variety of photovoltaic devices.[24–26] Application of this type of anti-reflection (AR) strategy for optical materials such as glass, with index values ≈1.5, is, however, limited by the absence of materials with appropriate indices of refraction (ideal value for a single layer AR coating is $n \approx 1.2$). One solution involves materials with homogeneously distributed nanopores as air voids, to reduce the index of refraction of the medium in an averaged sense. Approaches to realize such porous structures include phase separation and etching processes,[27–32] oblique angle deposition,[26,33–37] sol–gel techniques,[38–43] and sacrificial organic pore generators (e.g., dendrimers and amphiphilic block copolymers).[44–51] In all cases, the pores must have dimensions significantly smaller than the wavelengths of sunlight to avoid the detrimental effects of scattering,[52] which can be particularly problematic for CPV applications. An alternative approach relies on conical features of relief with sub-wavelength lateral dimensions, to create an effective spatial gradient in index and an associated smooth optical transition from the air to the substrate. Such textured surfaces can be created on silicon (Si) solar cells using standard etching techniques, with reflection losses typically below 1% across a broad range of the solar spectrum.[53–60] The formation of similar structures on the curved surfaces of glass or polymer optics in CPV technologies is, by comparison, highly challenging.

We describe herein materials approaches to broadband AR coatings that rely on single or dual layers of low index nanoporous spin-on-glasses formed using block copolymers and self-assembly, a process that has been widely studied to create low-k materials for applications in microelectronics.[61] The ability to adjust the index over a wide range, the excellent optical properties and the ease of formation of these coatings on flat and curved surfaces, in single or multilayer geometries, represent key attractive features. Specifically, the material consists of a dielectric matrix with a templating agent—an amphiphilic block copolymer that self-assembles into nanospheres—that can be removed in a thermal process that simultaneously transforms the matrix into a silica-like form with dispersed pores that have diameters (≈12 nm) far below values that could lead to light scattering or other disruptions in the optical path needed for effective concentration.[44,45,47,49,50,62] The molecular weight of the copolymer, and its relative concentration, define the sizes and densities of the pores, thereby providing deterministic control over the index of refraction. Single- and dual-layer coatings of this nanoporous anti-reflection (nAR) silica material yield optical performance in quantitative agreement with modeling. The resulting transmission values exceed ≈98% for wavelengths between 350 nm to 1.5 μm over angular ranges of up to ±40°, relevant to the most aggressive concentrating optics used in commercial CPV systems. As a functional demonstration, the application of optimized coatings onto the front and back side surfaces of plano-convex lenses for concentrating light onto microscale triple junction (3J) solar cells improves the short-circuit current values by 8.2%. The results suggest opportunities not only in PV but also in other photonic and optoelectronic devices, such as light-emitting diodes, imaging devices, display components, and optical sensors.

2. Results and Discussion

The chemistry and processing approaches (**Figure 1**A) followed procedures described previously.[47] Poly(methyl silsesquioxane) (PMSSQ, yellow) served as a matrix dielectric material and poly(styrene-*b*-2-vinylpyridine) (PS-*b*-P2VP, Mn: PS(7800)-P2VP(10000), red and blue represent PS and P2VP blocks, respectively) acted as a sacrificial templating agent. Upon spin casting and curing a mixture of these two components at elevated temperatures (120 °C for 3 h and 350 °C for 1 h), the Si—OH groups in the PMSSQ crosslinked to form Si—O—Si bonds, thereby transforming the matrix from hydrophilic to hydrophobic. This process also induced a phase separation of the PS-*b*-P2VP into core–shell nanospheres that exposed the hydrophobic PS block to the PMSSQ matrix, minimizing unfavorable interactions between P2VP and PMSSQ (Figure 1A). A pyrolysis step at 400 °C under an inert atmosphere removed the PS-*b*-P2VP (see Figure S1 in the Supporting Information for thermogravimetric analysis data), resulting in an organically modified silica dielectric matrix with spherical pores that had diameters of 12.2 ± 3.0 nm, as shown in the top-view scanning-electron microscopy (SEM) image (Figure 1B). The molecular weight of the PS-*b*-P2VP defined the sizes of these pores to values smaller than the wavelengths of terrestrial solar radiation (280–2500 nm). Hence, the nanoporous structure can be effectively regarded as a homogeneous medium with an effective refractive index (n) described by the Maxwell–Garnett model[47]

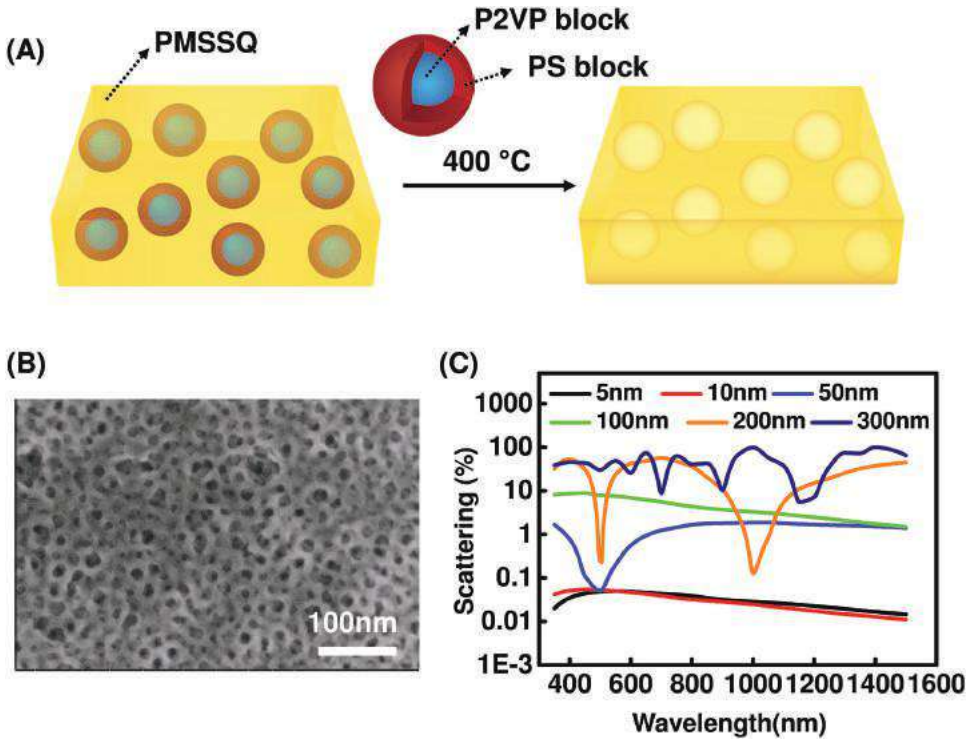

Figure 1. A) Schematic illustration of the formation of nanoporous, organically modified silica films: core (P2VP, blue)–shell (PS, red) polymer spheres were formed in the PMSSQ matrix (yellow) before being removed during a pyrolysis step to create the nanoporous structure. B) A top-view SEM image of a single-layer nanoporous film (brighter region represents the PMSSQ matrix). C) Simulated scattering for light transmission through such films as a function of characteristic pore diameter.

$$\frac{n^2-1}{n^2+2}=(1-\Delta p)\frac{n_{\mathrm{MSSQ}}^2-n_{\mathrm{air}}^2}{n_{\mathrm{MSSQ}}^2+2n_{\mathrm{air}}^2} \quad (1)$$

where Δp is the porosity of the structure, and n_{MSSQ} and n_{air} represent the refractive indices of the PMSSQ matrix and air, respectively.

The small dimensions of the pores minimized scattering losses, thereby maximizing the amount of direct sunlight that can be effectively focused onto the MJ cells. Simulations (COMSOL, Inc.) can capture the dependence of scattering on dimensions for operation across the solar spectrum, as shown in Figure 1C. The scattered field decreased rapidly to negligible levels for pore sizes below 50 nm, in a manner consistent with a reduction proportional to the sixth power of the size, as expected in the Rayleigh regime (i.e., $x\left(=\frac{\pi d}{\lambda}\right) << 1$ where d is the diameter of the pore and λ is the wavelength). For sizes comparable to the wavelength of incident light (i.e., d >100 nm), a transition from Rayleigh to Mie scattering occurred with characteristic oscillating behaviors, as solutions to Maxwell's equations in the Mie regime take the form of an infinite series of spherical waves represented by Bessel functions. The total amount of scattering (weighted against the Air Mass (AM) 1.5G spectrum) also increased dramatically in this regime, from 0.034% for $d = 10$ nm to 44.2% for $d = 300$ nm. For all cases reported here, appropriate choices of the molecular weight of PS-*b*-P2VP yielded $d \approx 12$ nm in a very simple, but well-controlled process. Such dimensions in lithographically defined structures, such as those required for sub-wavelength surfaces, would be difficult to achieve.

The properties of these nanoporous films were examined as coatings on flat substrates, with their refractive indices and thicknesses controlled by PS-*b*-P2VP loading and solution concentration (and spin speed), respectively (Figure S2, Supporting Information). **Figure 2**A presents a cross-sectional SEM image of a single-layer film (PS-*b*-P2VP loading ≈48%, index ≈1.2) on a Si wafer. The flatness, uniformity and pore-size distributions of the film have been described elsewhere.[47] Calculations based on the transfer matrix method[63–65] (see the Experimental section for details) defined optimal values of the thickness (t) and refractive index (n) for AR performance on a glass substrate across a broad solar spectral range from 350 nm to 1.5 μm, corresponding to the operation of a typical 3J solar cell. Figure 2B provides a calculated contour plot of the average transmission (T_{avg}) from 350 nm to 1.5 μm as a function of n and t. A value of $T_{\mathrm{avg}} > 98\%$ can be achieved when $n = 1.15$–1.31 and $t = 85$–200 nm. By selecting the appropriate PS-*b*-P2VP loading, a film with features within this optimum range (n = 1.24, t = 122 nm), as measured by spectroscopic ellipsometry (VASE, J. A. Woollam Co.) was spin cast (2000 rpm for 30 s) onto a glass substrate in both single-side and double-side configurations. Figure 2C shows the transmission spectra measured by a spectrometer (Varian Cary 5G) for a bare, flat glass plate (black) and for glass with an nAR coating on one side (red) and on both sides (blue). The results quantitatively correspond to simulation results conducted by the transfer matrix method (Figure 2D). The measurements indicate that the double-sided case has a transmission (T) of 98.5% at a target wavelength (600 nm, where irradiance peaks in the standard solar spectrum), significantly higher

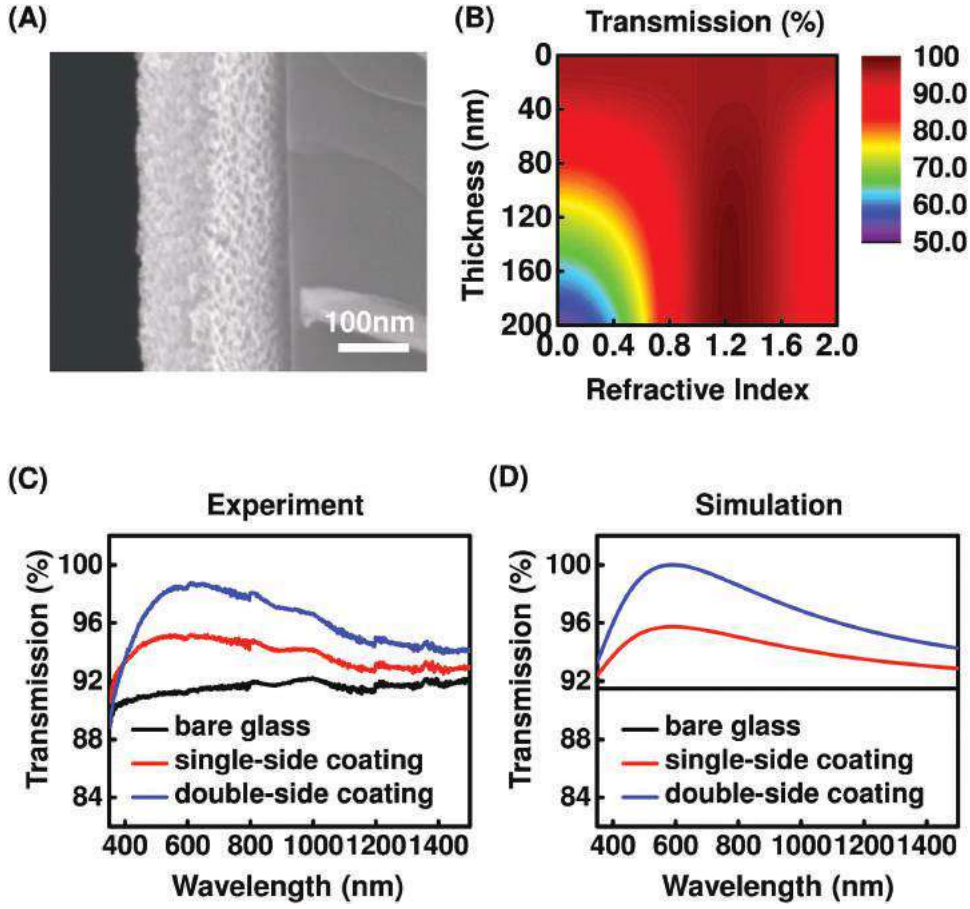

Figure 2. A) A cross-sectional SEM image of a single-layer nanoporous film. B) Calculated contour plot of the transmission averaged from 350 nm to 1.5 µm for a single-layer nAR film as a function of the refractive index and the thickness. C) Measured and D) simulated transmission spectra of a single-layer nanoporous coating at normal incidence for bare (black), single-side (red) and double-side (blue) cases.

than that of bare glass (T = 91.3%) or of glass with a single-side coating (T = 95.0%). The coated film showed a uniform thickness and index distribution, both of which are within the optimal ranges shown in Figure 2B, as determined by the ellipsometry measurement (Figure S3, Supporting Information). The spectral range of such single layer nAR coatings is, however, still narrower than that desired for operation of advanced MJ cells. The double-layer nAR coatings described in the following section address this issue.

For the bilayer coatings, transfer matrix calculations were used to determine the optimal values for both the refractive index (n_1 and n_2, denoting the top and bottom layer, respectively) and the thickness (t_1 and t_2) of each layer. **Figure 3**A presents a calculated contour plot of T_{avg} between 350 nm to 1.5 µm as a function of n_1 and n_2, when $t_1 = t_2 = 120$ nm. The results indicate that $T_{avg} > 99\%$ is possible when $n_1 = 1.08–1.22$ and $n_2 = 1.23–1.39$. The thicknesses of the two layers can be optimized for fixed refractive indices ($n_1 = 1.15$ and $n_2 = 1.31$), as presented in Figure 3B. The optimal ranges were calculated to be $t_1 = 100–180$ nm and $t_2 = 90–160$ nm. The formation of a double-layer film ($n_1 = 1.12$, $n_2 = 1.34$, $t_1 = 108$ nm, $t_2 = 103$ nm) began with the formation of a base layer (with a higher index) using the procedures described above. Exposure to ultraviolet (UV) induced ozone then produced —OH groups that improved the wettability of the film for spin casting a MSSQ/PS-*b*-P2VP precursor solution to define the top layer. Figure 3C provides the measured transmission spectra of such double-layer nAR coated glass samples at normal incidence, exhibiting excellent agreement with simulated transmission data shown in Figure 3D. The data obtained from the single-layer nAR coated samples are displayed in the same plot as dashed lines. As evidenced by both the simulated and experimental results, a remarkably improved spectral coverage was achieved with the double-layer configuration (measured T_{avg} = 98.2%) as compared to the single-layer case (measured T_{avg} = 96.1%). Such highly efficient transmission over wavelengths spanning the solar spectrum is suitable for use with MJ solar cells, as validated in the last section of this paper.

The performance of these nAR coatings across a range of angles of incidence is important to their use on lens surfaces in CPV modules. For instance, for the microlens arrays (f# ≈ 2) used in certain commercial CPV modules (Semprius), sunlight with normal incidence strikes the edges of the optics at an angle of nearly 40° (see Figure S4 in the Supporting Information). For advanced hybrid CPV modules that enable the capture of diffuse light,[22] the effective angles of incidence could even exceed this value. **Figure 4** presents measured and simulated angle-resolved transmission spectra under unpolarized

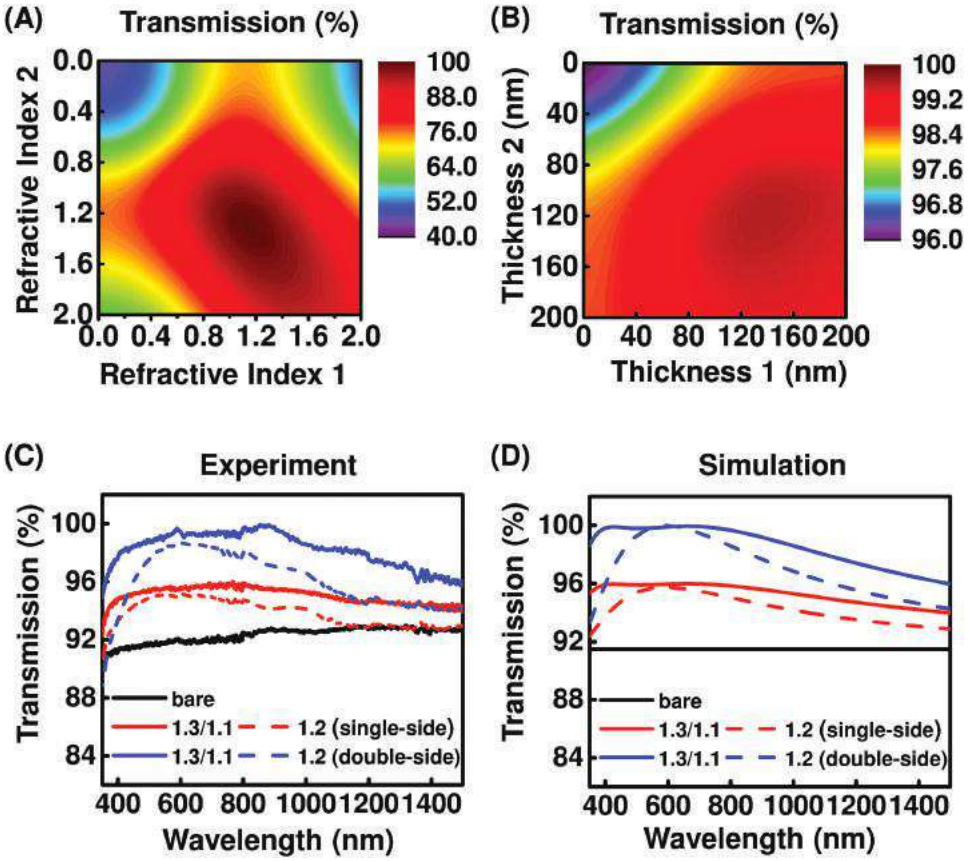

Figure 3. Calculated contour plots of the average transmission as a function of A) refractive indices of bilayers at fixed thicknesses of $t_1 = t_2 = 120$ nm and B) thicknesses at fixed refractive indices of $n_1 = 1.15$ and $n_2 = 1.31$. C) Measured and D) simulated transmission spectra of double-layer nanoporous coatings at normal incidence for bare (black), single-side (red) and double-side (blue) cases. For ease of comparison, this plot also includes results for the single-layer coating.

illumination for a flat glass substrate with a double-sided nAR coating in both single-layer (Figure 4A,B) and double-layer (Figure 4C,D) configurations. The experimental data were taken using an ellipsometer, while the simulations were performed using the finite-element based method (COMSOL Multiphysics software). Figure S5 in the Supporting Information shows the measured angle-dependent transmission of the control sample without nAR coatings. Compared to the single-layer coatings, the double-layer case offered increased angular bandwidth and improved transmission, as expected due to the gradient refractive index profile of the nAR bilayer. For incident angles up to 40°, T_{avg} was ≈98% between 350 nm and 1.5 µm for the sample with the double-layer coating. The measured and simulated angle-dependent spectral results for p- and s-polarizations are presented in Figure S6 (single layer) and Figure S7 in the Supporting Information (double layer), showing an insensitivity to polarization up to 40°. Such angle- and polarization-insensitive properties of these nAR films arose primarily from very weak optical interference effects due to a small index contrast between the nAR layer and the air/substrate, thereby leading to a broad resonance with a poor quality factor (Q-factor). Although the resonant wavelength shifted slightly toward shorter wavelengths with increasing angle of incidence, a typical observation in many cavity systems, the ample breadth of the resonance minimized these effects. In multilayer AR coatings (e.g. Bragg mirrors), strong optical interference effects can occur at certain wavelengths, resulting in significant variations in performance with angle. In addition to the broad resonance, the randomly distributed pores also promote angle-invariant characteristics as compared to traditional AR schemes that use periodic structures, in which photonic resonances and/or diffraction effects result from the periodic nature of these systems.[54,66]

Applying nAR coatings to both sides of the primary plano-convex lens surfaces in a CPV measurement set up (see **Figure 5**A) demonstrated their utility in this type of application. The processing used spin coating and pyrolysis steps described earlier, yielding sufficient uniformity in film thickness to maintain the high-transmission performance observed on flat substrates (see Figure S8 in the Supporting Information). Figure 5B presents optical images of the samples with (top) and without (bottom) the nAR coating on both sides, clearly showing that the coated lens exhibited notably reduced reflections as compared to the bare lens. The PV performance characteristics measured with a solar microcell 3J (InGaP/GaAs/InGaAsNSb, 1.9/1.4/1.0 eV) under simulated AM 1.5G solar irradiance (the experimental configuration is provided in Figure 5A, concentration ratio 50×) shows a relative photo-current enhancement of 6.0% and 8.2% with the single- (n = 1.24, t ≈ 120 nm) and

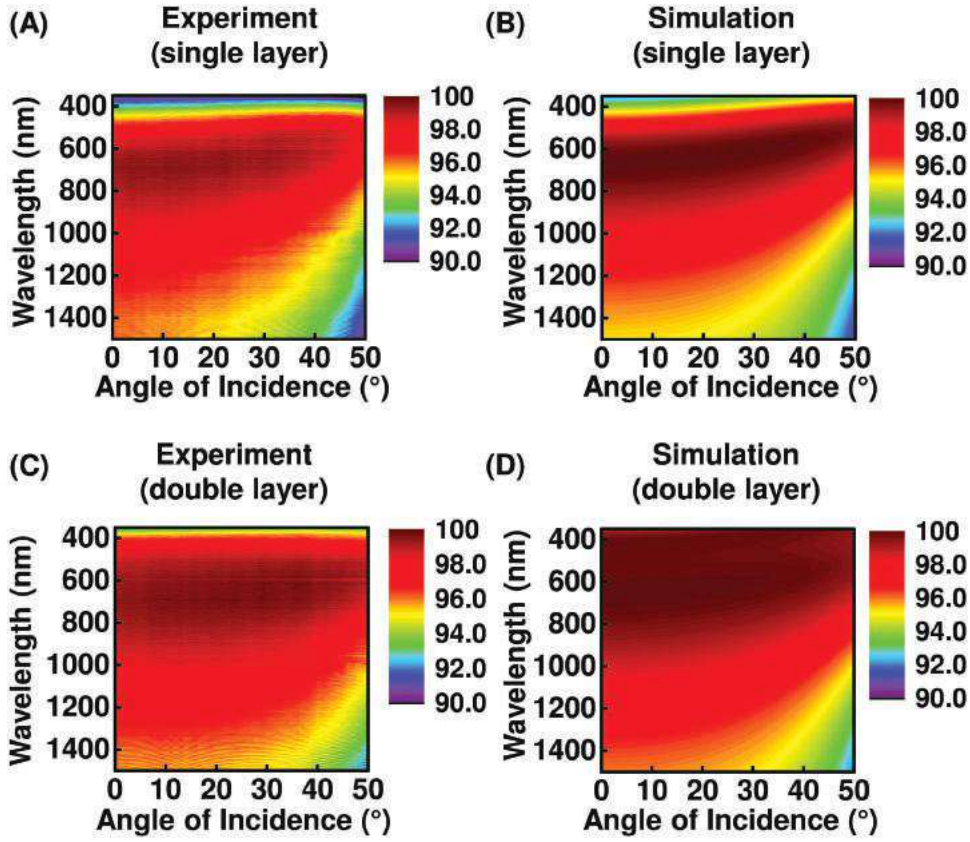

Figure 4. Measured and simulated angle-resolved transmission spectra of A,B) single-layer and C,D) double-layer nanoporous coatings under unpolarized light illumination. Optical properties of the nanoporous film were only weakly sensitive to angle of incidence up to 40°. The spectral range of operation increased with the introduction of an additional layer (i.e., bilayer configuration) with optimal refractive indices.

double-layer (n_1 = 1.12, n_2 = 1.34, $t_1 \approx$ 100 nm, $t_2 \approx$ 100 nm) nAR coatings, respectively (Figure 5C). These current enhancements matched well with the calculated transmission enhancements measured on flat glass substrates (5.8% for single-layer coating and 7.1% for double-layer coating, as weighted against the AM 1.5G spectrum). The difference can be explained by the slightly higher Fresnel losses on curved lens surfaces and solar simulator spectrum/intensity variations. Based on the energy conversion efficiency (35.5%) of the CPV module (1000×) that employs the same type of 3J cells,[67] the absolute module efficiency gain is estimated to be 2.9% when applying the double-layer coating on the large-area lens array.

3. Conclusion

A low-dielectric-constant AR coating material featuring a nanoporous structure composed of subwavelength pores enabled tunable index of refraction, in single or multilayer coatings, with excellent optical transmission properties and minimal light scattering. The index of refraction can be selected in the range between 1.1 and 1.4 by control over the sacrificial polymer loading. An AR coating with a double-layer configuration and a gradient refractive index profile (n_1 = 1.12, n_2 = 1.34) on a glass substrate (n = 1.5) led to transmission efficiency higher than 98% over a broad spectral range from 350 nm to 1.5 µm, with high angular performance up to ±40°. Exploiting the double layer AR scheme on the curved surfaces of concentrating optics in CPV technologies led to an 8.2% improvement in the current from 3J microcells, translating to a nearly 3% enhancement in the absolute CPV module efficiency. This approach has the potential to produce substantial performance enhancements in a wide variety of applications, including light-emitting diodes, solar cells, geometric optics, and display components. Future work focuses on the development of low temperature processing procedures as well as fabrication methods (e.g., aerosol spray) that would enable application on large area or highly curved surfaces (e.g., ball lens) with high throughput and uniformity.

4. Experimental Section

Nanoporous Anti-Reflection Coating Fabrication: The single layer nAR films were prepared by dissolving PS-*b*-P2VP (Polymer Source) and PMMSQ (GR650F, Techneglas) mixtures in tetrahydrofuran and spinning onto pre-cleaned substrates (Si wafer, coverslip glass, or lens) at 2000 rpm for 30 s, where the refractive index and film thickness were controlled by PS-*b*-P2VP loading and solution concentration, respectively. The coated substrate was then baked in a tube furnace with flowing N_2 first at 120 °C for 3 h, then ramped to 350 °C for 1 h, followed by 400 °C for 3 h before slowly cooling down to room temperature. The

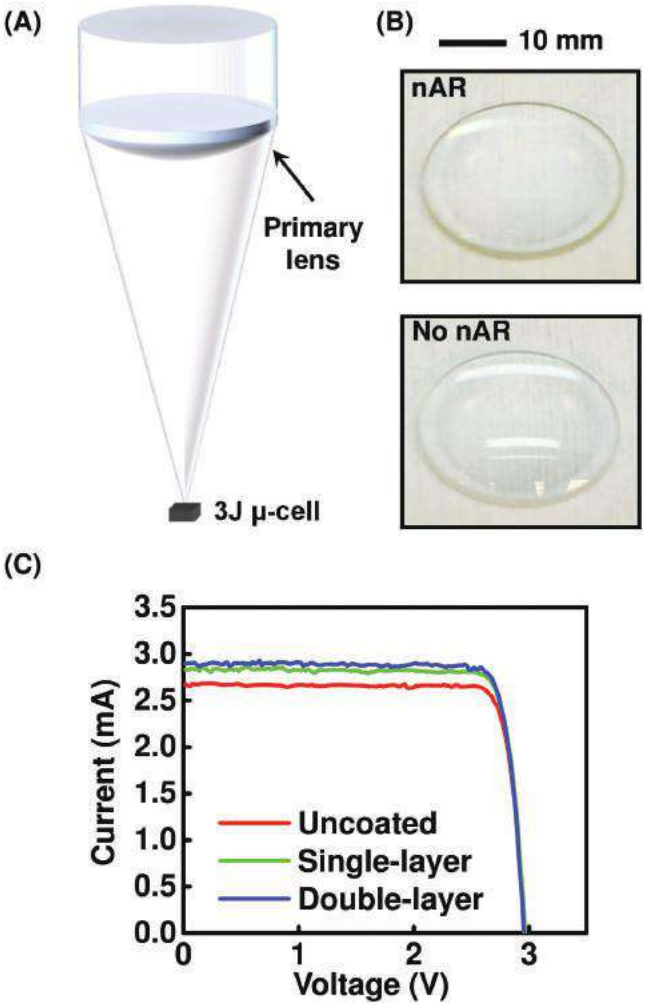

Figure 5. A) Schematic illustration of incident light focusing onto a 3J solar cell through a primary plano-convex lens. B) Optical images of a plano-convex lens with (top) and without (bottom) nAR coatings on both sides, revealing the suppression of reflections in the former case. C) PV performance of the 3J solar cells (InGaP/GaAs/InGaAsNSb, 1.9/1.4/1.0 eV) without (red) and with single-layer (green) and double-layer (blue) nAR coatings. The relative enhancement in short-circuit current was 8.2% for the latter case.

ramp rate was set to be 1 °C min^{-1}. For double layer coatings, after fabrication of the bottom layer, the surface was treated with ozone using a ultraviolet ozone cleaning system (UVOCS) for 2 min before spinning the top layer to ensure proper adhesion. The PMSSQ in the bottom layer switched from hydrophilic to hydrophobic after curing, which also hindered the infiltration of the top layer solution during fabrication and prevented the infill of the bottom layer pores. SEM images of the nAR films were obtained on Helios 600i and JEOL 7000F Scanning Electron Microscopes.

Optical Simulations and Characterizations: Optical simulations to explore scattering properties and angular dependence of the nanoporous structure were carried out using finite-element method with the commercial COMSOL Multiphysics software. A scattering boundary condition was used for both surfaces of incident medium and a substrate, while a periodic boundary condition was used for side surfaces of the nanoporous structure. In order to absorb multiple reflections and transmissions, the effective simulation domain of the entire structure was circumscribed by a perfectly matched layer. The scattering was calculated by integrating the outward-going far-field time average scattered power through a closed surface surrounding a nanoporous medium. Two different built-in mesh parameter sets in COMSOL Multiphysics were used when meshing the entire geometry. For a porous medium with subwavelength features, *Extremely fine* was used to mesh the geometry ensuring that the mesh size was much smaller than the nanopores, whereas *Normal* was used for the rest of media that were homogeneous and isotropic.

Optimal ranges of the refractive index and the film thickness for single- and double-layer nAR coatings were calculated by using the transfer matrix method, based on Maxwell equations and the continuity of the electric field parallel to the boundaries between two homogeneous media with different refractive index. Given the electric field at the end of the first medium (E_{1+} and E_{1-}, "+" and "–" denotes two propagation directions), the electric field at the end of the second layer (E_{2+} and E_{2-}) can be simply derived through a simple matrix operation, where both interface reflections and propagation through the second medium are represented by two separate 2×2 matrices (D_{12} and P_2, respectively, E' denotes the electric field at the start of one medium)

$$\begin{pmatrix} E_{1+} \\ E_{1-} \end{pmatrix} = D_{12} \begin{pmatrix} E'_{2+} \\ E'_{2-} \end{pmatrix} = D_{12} P_2 \begin{pmatrix} E_{2+} \\ E_{2-} \end{pmatrix} \tag{2}$$

The electric field after a stack of layers (E'_{N+} and E'_{N-}, where $E'_{N-} = 0$) can then be calculated by multiplying the individual layer matrices

$$\begin{aligned} \begin{pmatrix} E_{1+} \\ E_{1-} \end{pmatrix} &= D_{12} P_2 \begin{pmatrix} E_{2+} \\ E_{2-} \end{pmatrix} = D_{12} P_2 D_{23} P_3 \begin{pmatrix} E_{3+} \\ E_{3-} \end{pmatrix} \\ &= D_{12} P_2 D_{23} P_3 \cdots P_{N-1} D_{(N-1)N} \begin{pmatrix} E'_{N+} \\ E'_{N-} \end{pmatrix} \\ &= \begin{pmatrix} M_{11} & M_{12} \\ M_{21} & M_{22} \end{pmatrix} \begin{pmatrix} E'_{N+} \\ E'_{N-} \end{pmatrix} \end{aligned} \tag{3}$$

The reflection (R) and transmission (T) of the whole structure can then be obtained by the following equations

$$R = \left| \frac{E_{1-}}{E_{1+}} \right|^2 = \left| \frac{M_{21}}{M_{11}} \right|^2 \tag{4}$$

$$T = \left| \frac{E'_{N+}}{E_{1+}} \right|^2 = \left| \frac{1}{M_{11}} \right|^2 \tag{5}$$

Spectral transmittance curves at normal incidence were measured by using a spectrometer (Varian Cary 5G). The angle-resolved transmission spectra were obtained by a Focused RC2 spectroscopic ellipsometer (J. A. Woollam Co.). Refractive index and thickness of the nAR layers were determined by using ellipsometers (VASE and Focused RC2, J. A. Woollam Co.).

PV performance of the microscale 3J cell was characterized with a Keithley 2400 sourcemeter. The illumination source was an Oriel 91192-1000W Solar Simulator with an AM1.5G filter (calibrated to one sun, 100 mW·cm^{-2}). The concentrating optic used was an N-BK7 plano-convex lens (LA1102, Thorlabs, D = 30.0 mm, f = 50.0 mm), with or without dual-side nAR coatings. The position of the lens was accurately adjusted by a x–y–z manipulator to ensure proper optical alignment.

Supporting Information

Supporting Information is available from the Wiley Online Library or from the author.

Acknowledgements

Y.Y. and K.-T.L. contributed equally to this work. This work was supported by the "Light-Material Interactions in Energy Conversion" Energy Frontier Research Center funded by the U.S. Department of Energy, Office of Science, Office of Basic Energy Sciences under Award Number DE-SC0001293. X.S. acknowledges the support from National Natural Science Foundation of China (Project 51602172). M.M.H. acknowledges the support from King Abdullah University of Science and Technology (KAUST) Technology Transfer Office under Award No. GEN-01-4014. The authors thank B. Henderson (Sensofar), K. Walsh (UIUC), and J. C. Mabon (UIUC) for their assistance with materials characterization.

Received: September 7, 2016
Revised: October 14, 2016
Published online: December 6, 2016

[1] H. Cotal, C. Fetzer, J. Boisvert, G. Kinsey, R. King, P. Hebert, H. Yoon, N. Karam, *Energy Environ. Sci.* **2009**, *2*, 174.
[2] J. M. Gee, G. F. Virshup, *Proc. 20th IEEE Photovoltaic Spec. Conf.* **1988**, *1*, 754.
[3] L. M. Fraas, J. E. Avery, V. S. Sundaram, V. T. Dinh, T. M. Davenport, J. W. Yerkes, J. M. Gee, K. A. Emery, *Proc. 21st IEEE Photovoltaic Spec. Conf.* **1990**, *1*, 190.
[4] T. Takamoto, E. Ikeda, T. Agui, H. Kurita, T. Tanabe, S. Tanka, H. Matsubara, Y. Mine, S. Takagishi, M. Yamaguchi, *Proc. 26th IEEE Photovoltaic Spec. Conf.* **1997**, 1031.
[5] R. R. King, D. C. Law, K. M. Edmondson, C. M. Fetzer, G. S. Kinsey, H. Yoon, R. A. Sherif, N. H. Karam, *Appl. Phys. Lett.* **2007**, *90*, 183516.
[6] J. F. Geisz, S. Kurtz, M. W. Wanlass, J. S. Ward, A. Duda, D. J. Friedman, J. M. Olson, W. E. McMahon, T. E. Moriarty, J. T. Kiehl, *Appl. Phys. Lett.* **2007**, *91*, 023502.
[7] R. R. King, A. Boca, W. Hong, X. Liu, D. Bhusari, D. Larrabee, K. Edmondson, D. Law, C. Fetzer, S. Mesropian, *Proc. 24th Eur. Photovoltaic Sol. Energy Conf.* **2009**, *21*, 55.
[8] L. Zhao, G. Flamand, J. Poortmans, *AIP Conf. Proc.* **2010**, *1277*, 284.
[9] S. Wojtczuk, P. Chiu, X. Zhang, D. Pulver, C. Harris, B. Siskavich, *AIP Conf. Proc.* **2011**, *1407*, 9.
[10] D. Derkacs, R. Jones-Albertus, F. Suarez, O. Fidaner, *J. Photon. Energy* **2012**, *2*, 021805.
[11] K. Tanabe, K. Watanabe, Y. Arakawa, *Sci. Rep.* **2012**, *2*, 349.
[12] K. Sasaki, T. Agui, K. Nakaido, N. Takahashi, R. Onitsuka, T. Takamoto, *AIP Conf. Proc.* **2013**, *1556*, 22.
[13] X. Sheng, C. A. Bower, S. Bonafede, J. W. Wilson, B. Fisher, M. Meitl, H. Yuen, S. Wang, L. Shen, A. R. Banks, C. J. Corcoran, R. G. Nuzzo, S. Burroughs, J. A. Rogers, *Nat. Mater.* **2014**, *13*, 593.
[14] F. Dimroth, M. Grave, P. Beutel, U. Fiedeler, C. Karcher, T. Tibbits, E. Olivia, G. Siefer, M. Schachtner, A. Wekkeli, A. Bett, R. Krause, M. Piccin, N. Blanc, C. Drazek, E. Guiot, B. Ghyselen, T. Salvetat, A. Tauzin, T. Signamarcheix, A. Dobrich, T. Hannappel, K. Schwarzburg, *Prog. Photovoltaics: Res. Appl.* **2014**, *22*, 277.
[15] K. Derendorf, S. Essig, E. Oliva, V. Klinger, T. Roesener, S. P. Philipps, J. Benick, M. Hermle, M. Schachtner, G. Siefer, W. Jager, F. Dimroth, *IEEE J. Photovoltaics* **2013**, *3*, 1423.
[16] M. A. Green, K. Emery, Y. Hishikawa, W. Warta, E. D. Dunlop, *Prog. Photovoltaics: Res. Appl.* **2016**, *24*, 905.
[17] A. Polman, H. A. Atwater, *Nat. Mater.* **2012**, *11*, 174.
[18] C. N. Eisler, Z. e. R. Abrams, M. T. Sheldon, X. Zhang, H. A. Atwater, *Energy Environ. Sci.* **2014**, *7*, 3600.
[19] N. Yamada, K. Okamoto, *Opt. Express* **2014**, *22*, A28.
[20] N. Yamada, D. Hirai, *Prog. Photovoltaics: Res. Appl.* **2016**, *24*, 846.
[21] S. Boriskina, M. A. Green, C. Catchpole, E. Yablonovitch, M. C. B. Beard, Y. Okada, S. Lany, T. Gershon, A. Zakutayev, M. H. Tahersima, V. J. Sorger, M. J. Naughton, K. Kempa, M. Dagenais, Y. Yao, L. Xu, X. Sheng, N. D. Bronstein, J. A. Rogers, A. P. Alivisatos, R. G. Nuzzo, J. M. Gordon, D. M. Wu, M. D. W. Wisser, A. Salleo, J. Dionne, P. Bermel, J.-J. Greffet, I. Celanovic, M. Soljacic, A. Manor, C. Rotschild, A. Raman, L. Zhu, S. Fan, G. Chen, *J. Opt.* **2016**, *18*, 073004.
[22] K.-T. Lee, Y. Yao, J. He, B. Fisher, X. Sheng, L. Xu, M. A. Anderson, Y. Kang, A. Gumus, R. R. Bahabry, J. W. Lee, U. Paik, N. D. Bronstein, A. P. Alivisatos, M. Meitl, M. Lumb, S. Burroughs, M. M. Hussain, J. C. Lee, R. G. Nuzzo, J. A. Rogers, *Proc. Natl. Acad. Sci. USA* **2016**, doi: 10.1073/pnas.1617391113.
[23] E. Hecht, *Optics*, Addison Wesley, San Francisco **2002**.
[24] J. Zhao, A. Wang, P. Altermatt, M. A. Green, *Appl. Phys. Lett.* **1995**, *66*, 3636.
[25] D. Bouhafs, A. Moussi, A. Chikouche, J. M. Ruiz, *Sol. Energy Mater. Sol. Cells* **1998**, *52*, 79.
[26] S. Chhajed, M. F. Schubert, J. K. Kim, E. F. Schubert, *Appl. Phys. Lett.* **2008**, *93*, 251108.
[27] P. B. Clapham, M. C. Hutley, *Nature* **1973**, *244*, 281.
[28] M. J. Minot, *J. Opt. Soc. Am.* **1976**, *66*, 515.
[29] S. Walheim, E. Schäffer, J. Mlynek, U. Steiner, *Science* **1999**, *283*, 520.
[30] M. Ibn-Elhaj, M. Schadt, *Nature* **2001**, *410*, 796.
[31] Y. Du, H. He, Y. Jin, F. Kong, H. Guan, Z. Fan, *Appl. Surf. Sci.* **2012**, *258*, 6431.
[32] L.-Q. Liu, X.-L. Wang, M. Jing, S.-G. Zhang, G.-Y. Zhang, S.-X. Dou, G. Wang, *Adv. Mater.* **2012**, *24*, 6318.
[33] S. R. Kennedy, M. J. Brett, *Appl. Opt.* **2003**, *42*, 4573.
[34] J. Q. Xi, M. F. Schubert, J. K. Kim, E. F. Schubert, M. Chen, S.-Y. Lin, W. Liu, J. A. Smart, *Nat. Photonics* **2007**, *1*, 176.
[35] J. K. Kim, S. Chhajed, M. F. Schubert, E. F. Schubert, A. J. Fischer, M. H. Crawford, J. Cho, H. Kim, C. Sone, *Adv. Mater.* **2008**, *20*, 801.
[36] X. Yan, D. J. Poxson, J. Cho, R. E. Welser, A. K. Sood, J. K. Kim, E. F. Schubert, *Adv. Funct. Mater.* **2013**, *23*, 583.
[37] C. I. Yeo, H. J. Choi, Y. M. Song, S. J. Kang, Y. T. Lee, *J. Mater. Chem. A* **2015**, *3*, 7235.
[38] S. P. Mukherjee, W. H. Lowdermilk, *J. Non-Cryst. Solids* **1982**, *48*, 177.
[39] S. P. Mukherjee, W. H. Lowdermilk, *Appl. Opt.* **1982**, *21*, 293.
[40] P. Hinz, H. Dislich, *J. Non-Cryst. Solids* **1986**, *82*, 411.
[41] B. E. Yoldas, D. P. Partlow, *Thin Solid Films* **1985**, *129*, 1.
[42] D. R. Uhlmann, T. Suratwala, K. Davidson, J. M. Boulton, G. Teowee, *J. Non-Cryst. Solids* **1997**, *218*, 113.
[43] R. Prado, G. Beobide, A. Marcaide, J. Goikoetxea, A. Aranzabe, *Sol. Energy Mater. Sol. Cells* **2010**, *94*, 1081.
[44] C. V. Nguyen, K. R. Carter, C. J. Hawker, J. L. Hedrick, R. L. Jaffe, R. D. Miller, J. F. Remenar, H.-W. Rhee, P. M. Rice, M. F. Toney, M. Trollsås, D. Y. Yoon, *Chem. Mater.* **1999**, *11*, 3080.
[45] H. C. Kim, J. B. Wilds, C. R. Kreller, W. Volksen, P. J. Brock, V. Y. Lee, T. Magbitang, J. L. Hedrick, C. J. Hawker, R. D. Miller, *Adv. Mater.* **2002**, *14*, 1637.
[46] S. Yang, P. A. Mirau, C.-S. Pai, O. Nalamasu, E. Reichmanis, J. C. Pai, Y. S. Obeng, J. Seputro, E. K. Lin, H.-J. Lee, J. Sun, D. W. Gidley, *Chem. Mater.* **2002**, *14*, 369.
[47] C.-C. Yang, P.-T. Wu, W.-C. Chen, H.-L. Chen, *Polymer* **2004**, *45*, 5691.
[48] B. Lee, Y.-H. Park, Y.-T. Hwang, W. Oh, J. Yoon, M. Ree, *Nat. Mater.* **2005**, *4*, 147.
[49] K. Biswas, S. Gangopadhyay, H.-C. Kim, R. D. Miller, *Thin Solid Films* **2006**, *514*, 350.
[50] S. Kim, J. Cho, K. Char, *Langmuir* **2007**, *23*, 6737.
[51] H.-W. Su, W.-C. Chen, *Mater. Chem. Phys.* **2009**, *114*, 736.
[52] J. A. Hiller, J. D. Mendelsohn, M. F. Rubner, *Nat. Mater.* **2002**, *1*, 59.

[53] L. Philippe, G. M. Morris, *Nanotechnology* **1997**, *8*, 53.
[54] Y.-F. Huang, S. Chattopadhyay, Y.-J. Jen, C.-Y. Peng, T.-A. Liu, Y.-K. Hsu, C.-L. Pan, H.-C. Lo, C.-H. Hsu, Y.-H. Chang, C.-S. Lee, K.-H. Chen, L.-C. Chen, *Nat. Nanotechnol.* **2007**, *2*, 770.
[55] C.-H. Sun, P. Jiang, B. Jiang, *Appl. Phys. Lett.* **2008**, *92*, 061112.
[56] Q. Chen, G. Hubbard, P. A. Shields, C. Liu, D. W. E. Allsopp, W. N. Wang, S. Abbott, *Appl. Phys. Lett.* **2009**, *94*, 263118.
[57] S. A. Boden, D. M. Bagnall, *Prog. Photovoltaics: Res. Appl.* **2010**, *18*, 195.
[58] N. Yamada, O. N. Kim, T. Tokimitsu, Y. Nakai, H. Masuda, *Prog. Photovoltaics: Res. Appl.* **2011**, *19*, 134.
[59] X. Zhida, Y. Yuan, P. B. Eric, L. Lanfang, J. Jing, G. N. Ralph, L. Gang Logan, *Nanotechnology* **2014**, *25*, 305301.
[60] A. Rahman, A. Ashraf, H. Xin, X. Tong, P. Sutter, M. D. Eisaman, C. T. Black, *Nat. Commun.* **2015**, *6*, 5963.
[61] K. Maex, M. R. Baklanov, D. Shamiryan, F. Iacopi, S. H. Brongersma, Z. S. Yanovitskaya, *J. Appl. Phys.* **2003**, *93*, 8793.
[62] E. Huang, M. F. Toney, W. Volksen, D. Mecerreyes, P. Brock, H.-C. Kim, C. J. Hawker, J. L. Hedrick, V. Y. Lee, T. Magbitang, R. D. Miller, L. B. Lurio, *Appl. Phys. Lett.* **2002**, *81*, 2232.
[63] C. C. Katsidis, D. I. Siapkas, *Applied Optics* **2002**, *41*, 3978.
[64] E. X. Pérez, *Design, Fabrication and Characterization of Porous Silicon Multilayer Optical Devices*, Universitat Rovira i Virgili, Tarragona, Spain **2008**.
[65] M. C. Troparevsky, A. S. Sabau, A. R. Lupini, Z. Zhang, *Opt. Express* **2010**, *18*, 24715.
[66] R. H. Siddique, G. Gomard, H. Holscher, *Nat. Commun.* **2015**, *6*, 6909.
[67] Semprius' 35.5 Percent Efficiency Sets New Record for Commercially Available Solar Modules, **2013**.

ADVANCED ENERGY MATERIALS

Supporting Information

for *Adv. Energy Mater.,* DOI: 10.1002/aenm.201601992

Porous Nanomaterials for Ultrabroadband Omnidirectional Anti-Reflection Surfaces with Applications in High Concentration Photovoltaics

Yuan Yao, Kyu-Tae Lee, Xing Sheng, Nicolas A. Batara, Nina Hong, Junwen He, Lu Xu, Muhammad M. Hussain, Harry A. Atwater, Nathan S. Lewis, Ralph G. Nuzzo, and John A. Rogers**

Supporting Information

Porous Nanomaterials for Ultrabroadband Omnidirectional Anti-reflection Surfaces with Applications in High Concentration Photovoltaics

Yuan Yao,† Kyu-Tae Lee,† Xing Sheng, Nicolas A. Batara, Nina Hong, Junwen He, Lu Xu, Muhammad M. Hussain, Harry A. Atwater, Nathan S. Lewis, Ralph G. Nuzzo and John A. Rogers**

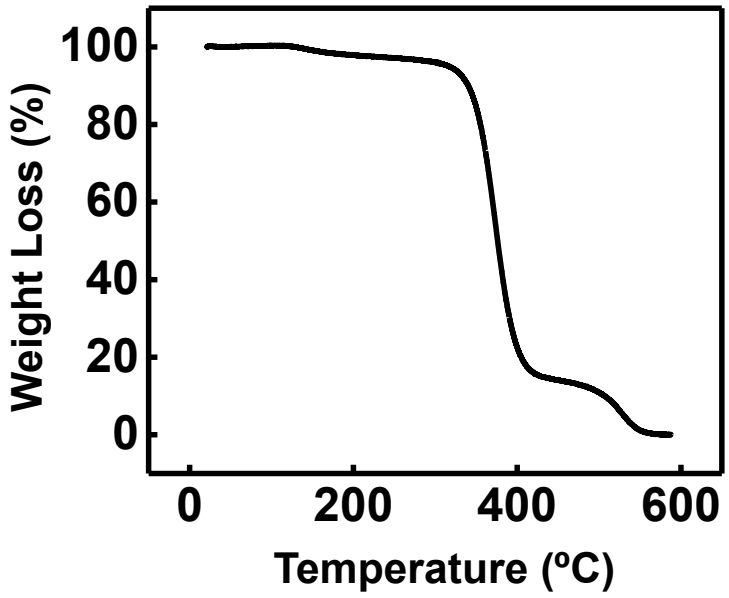

Figure S1. Thermogravimetric analysis data of PMMSQ/PS-*b*-P2VP mixture (65% PS-*b*-P2VP loading) measured by Q50-TGA at a temperature ramp rate of 5 ºC per minute.

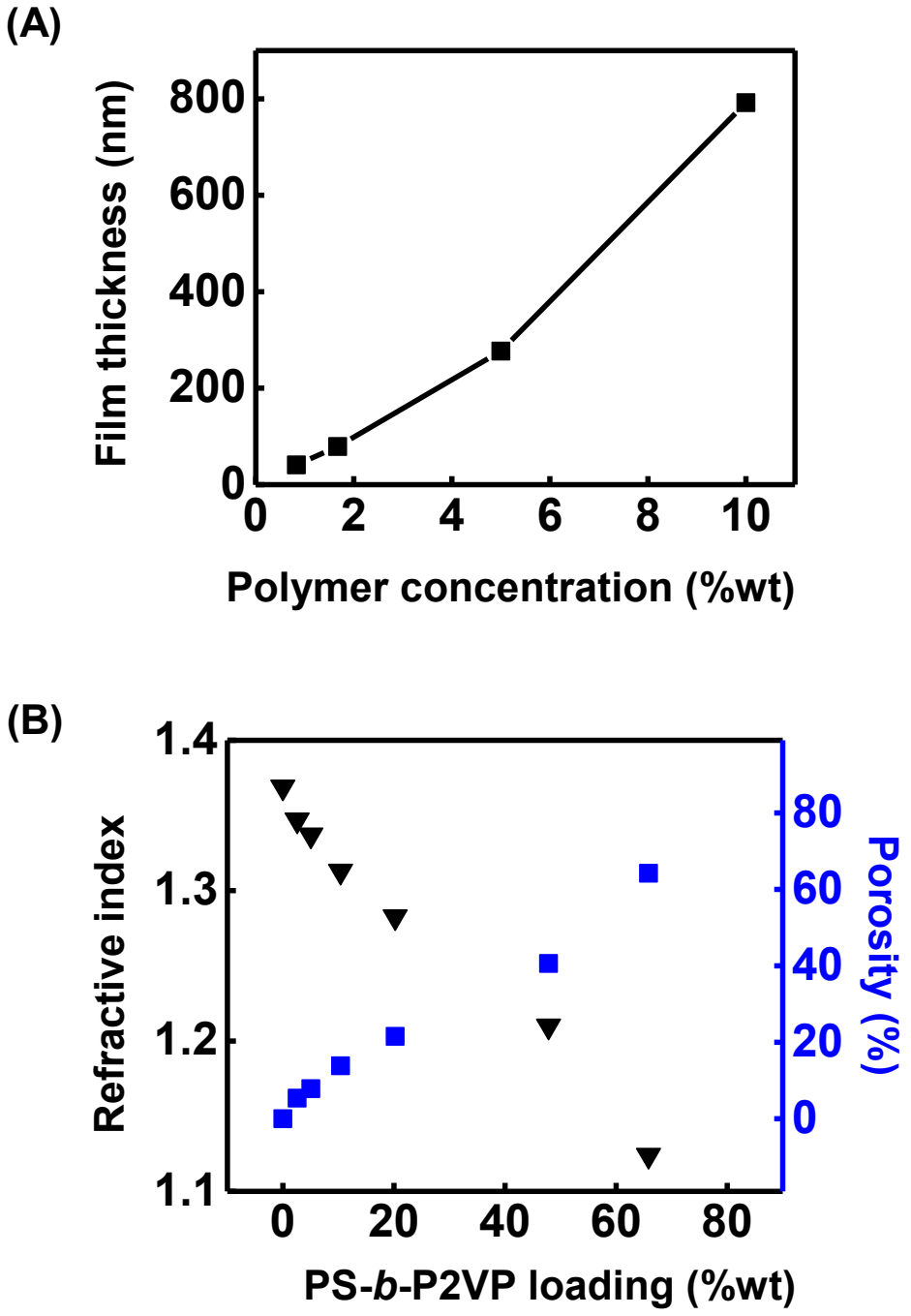

Figure S2. (A) Film thickness as a function of polymer mixture solution concentration (48% P2VP loading, with a spin-speed of 2000 rpm); (B) Refractive index (black triangles) and porosity (blue squares, calculated with Equation (1)) as a function of PS-*b*-P2VP loading.

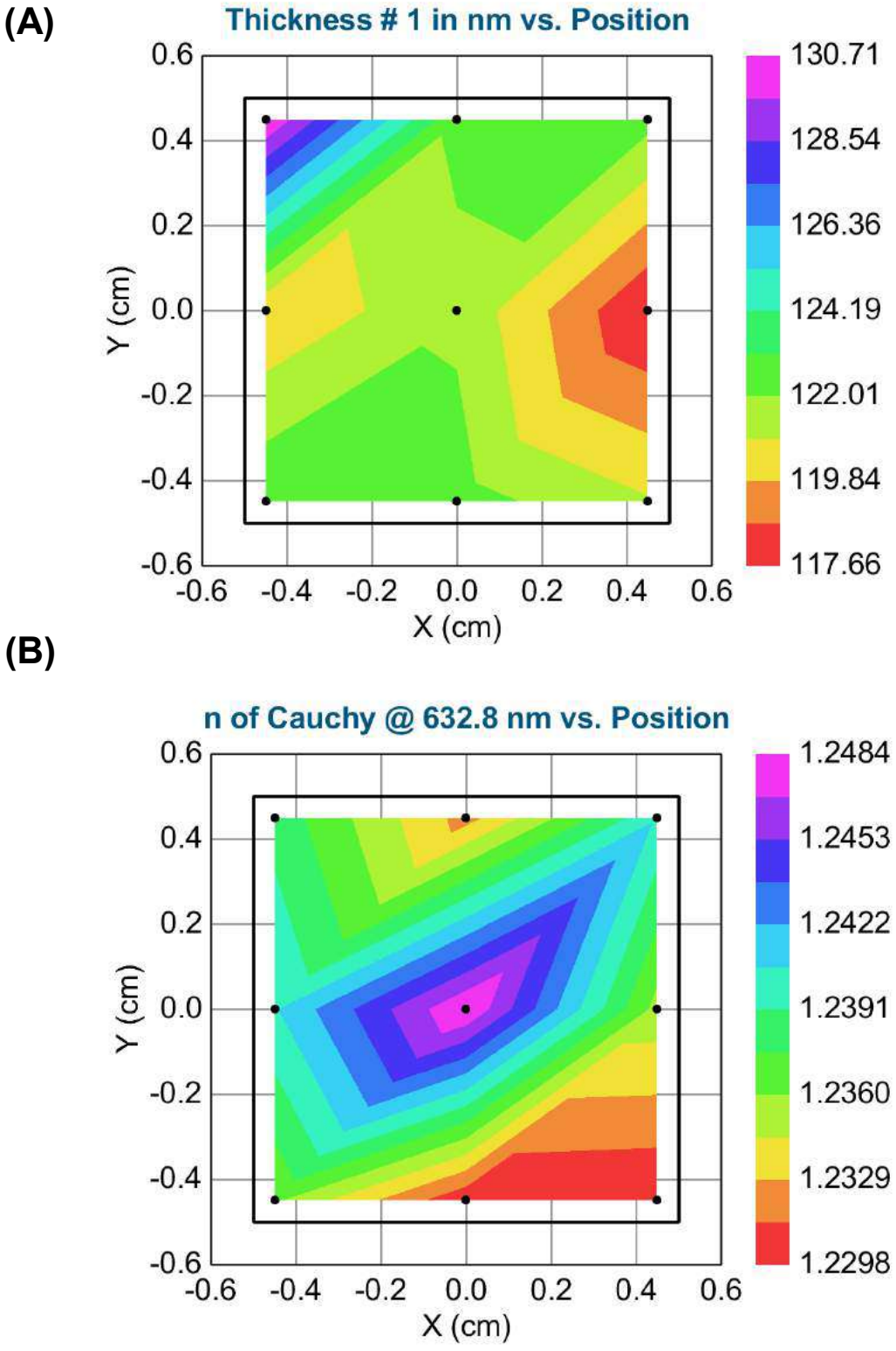

Figure S3. (A) Film thickness and (B) refractive index distribution on a single layer film coated on a glass substrate as mapped by a Focused RC2 spectroscopic ellipsometer.

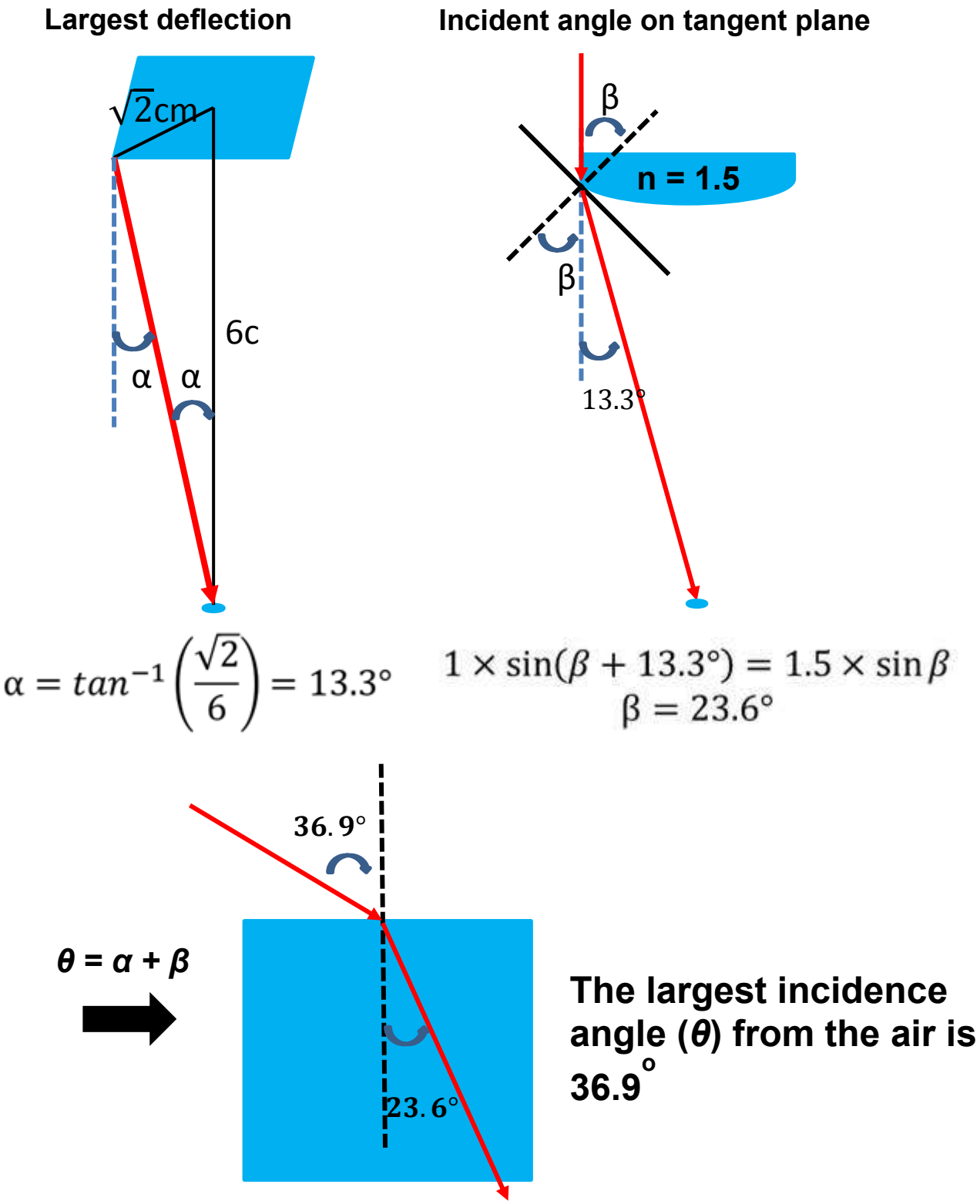

Figure S4. Calculations for the largest angle of incidence to consider for the lens unit in the commercial Semprius CPV module employing 3J cells.

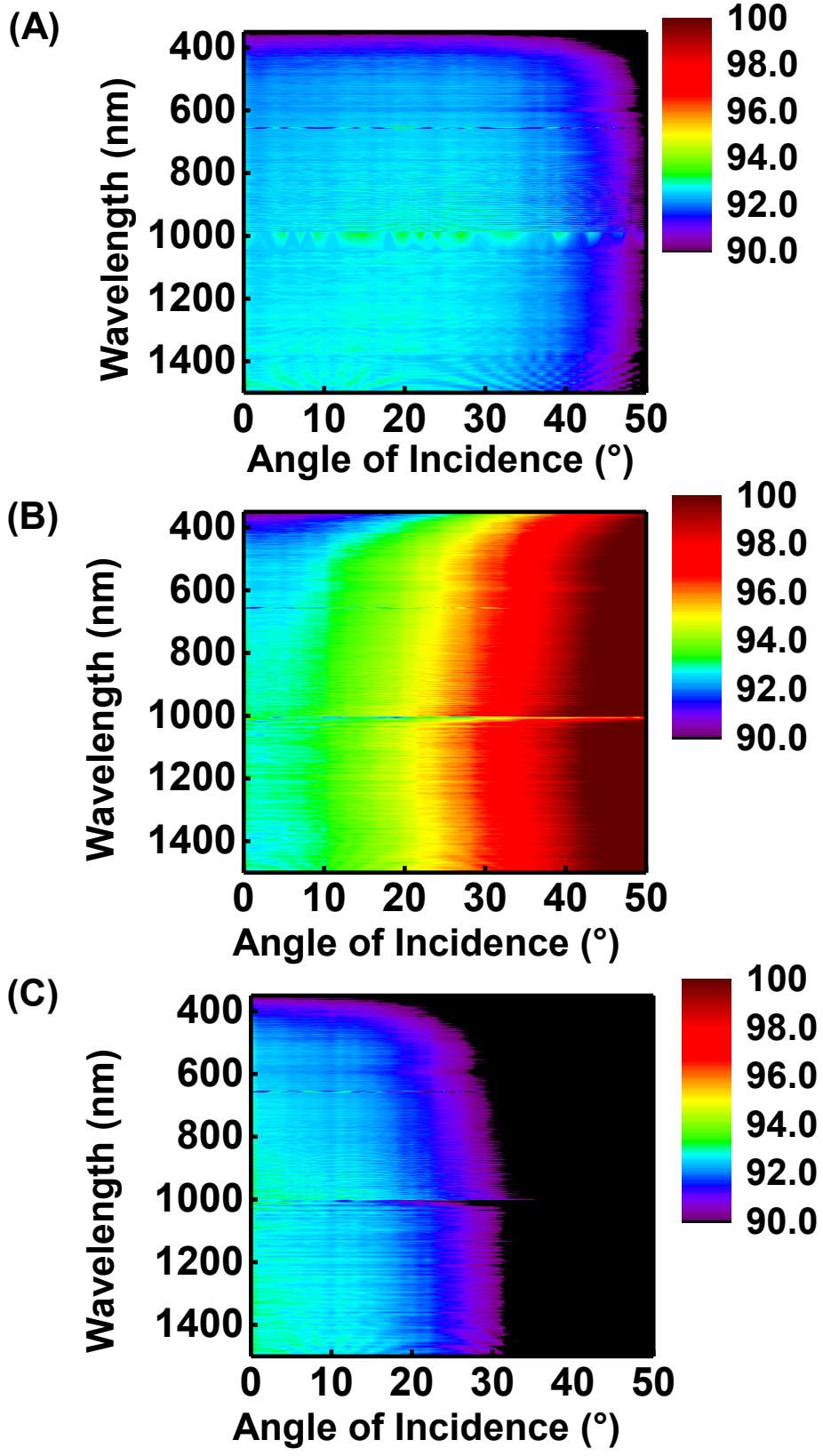

Figure S5. Measured angle-resolved transmission spectra for (A) unpolarized, (B) p- and (C) s-polarized light through a glass substrate (170 µm thick coverslip).

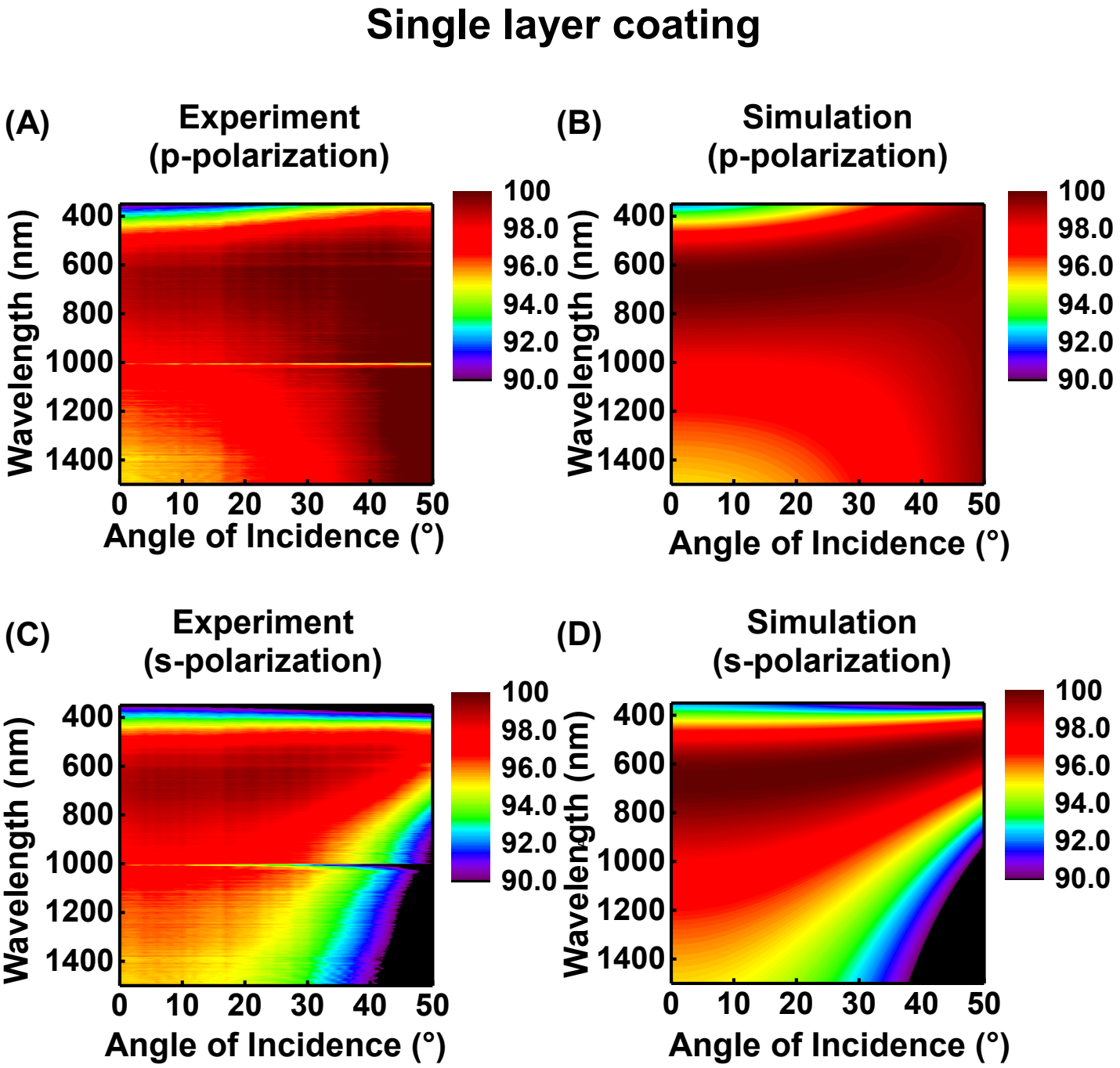

Figure S6. Measured and simulated angle-resolved transmission spectra of a glass substrate coated with a dual-side single-layer AR coating for (A, B) p- and (C, D) s-polarization.

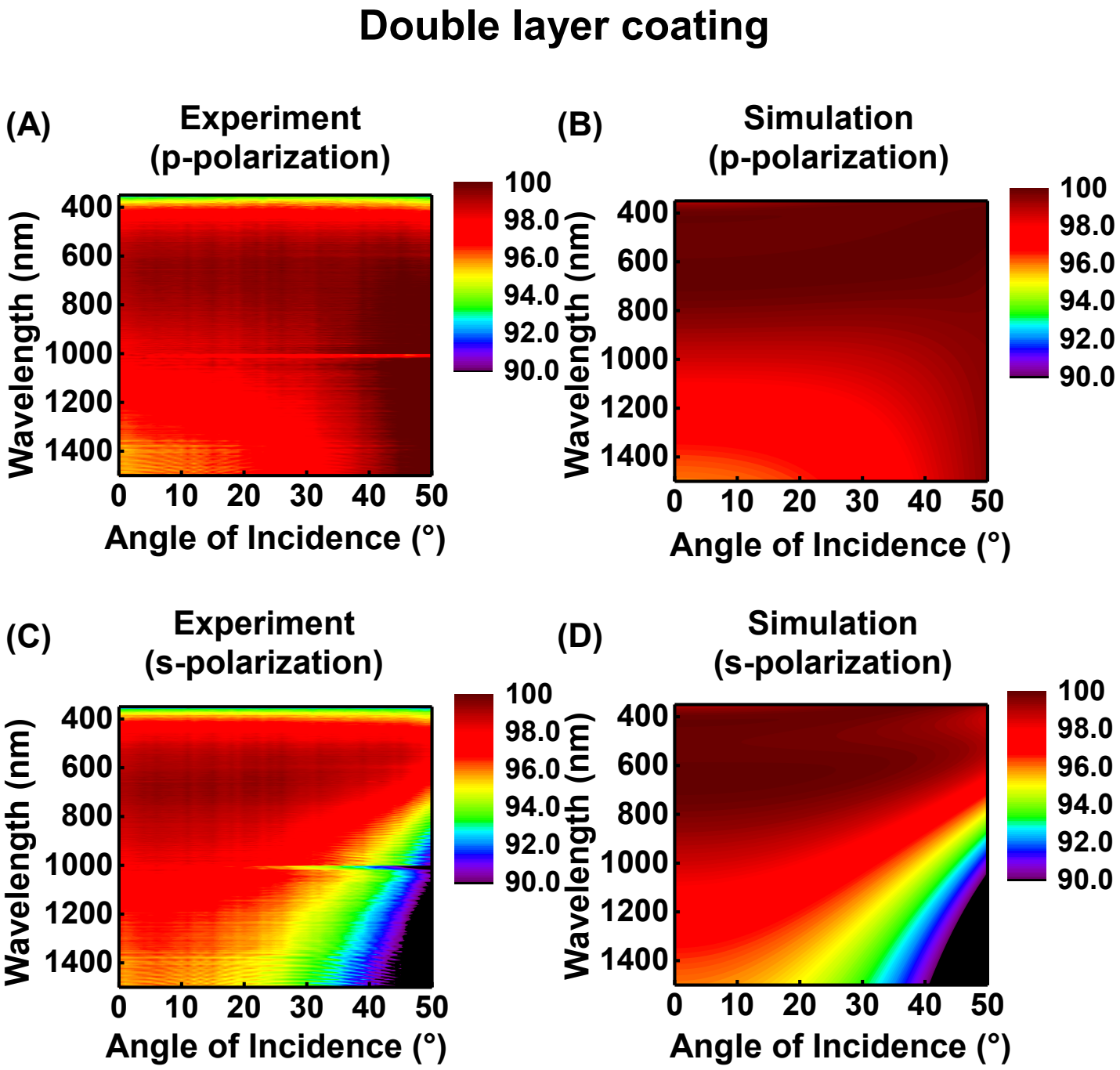

Figure S7. Measured and simulated angle-resolved transmission spectra of a glass substrate coated with a dual-side double-layer AR coating for (A, B) p- and (C, D) s-polarization.

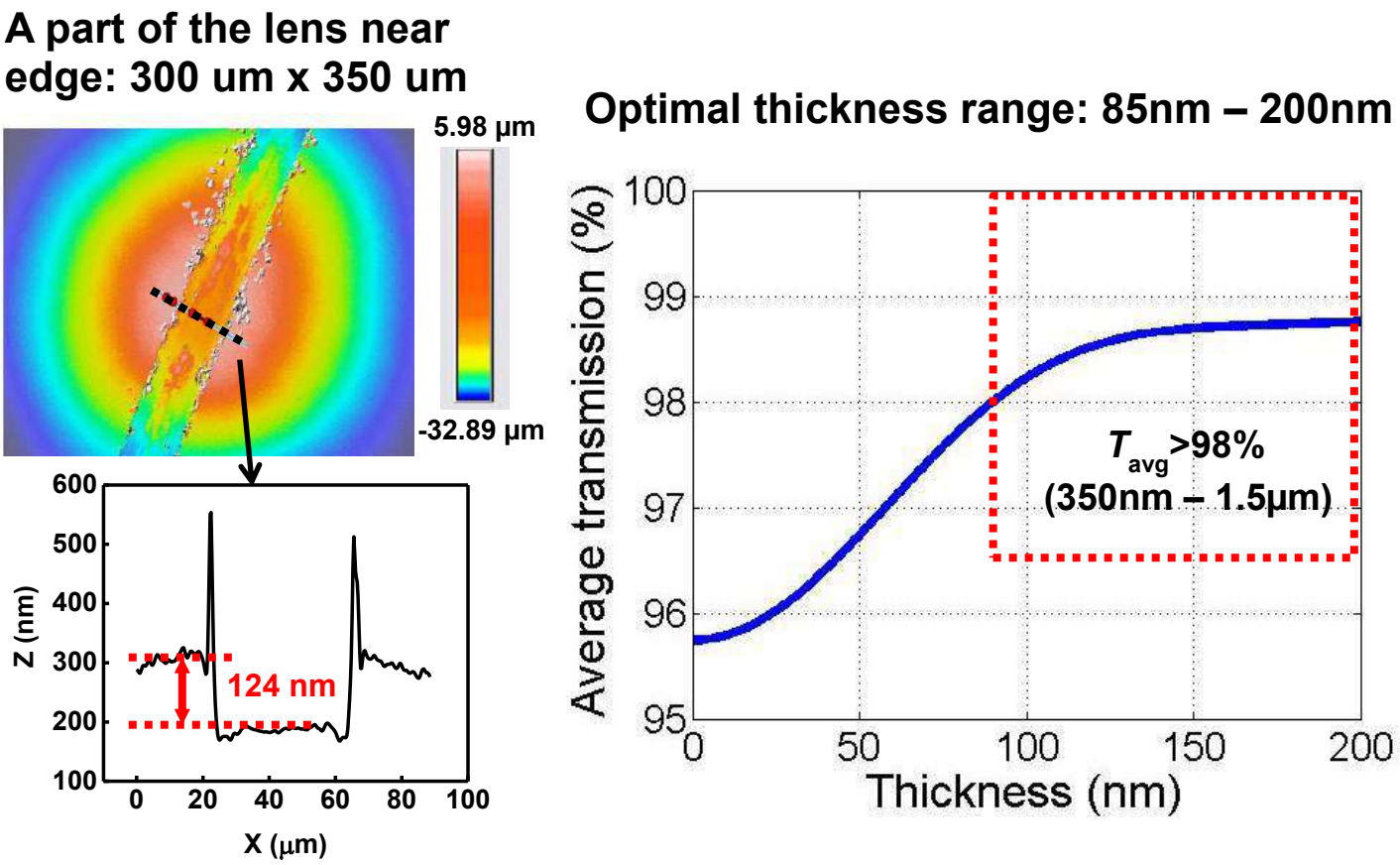

Measured film thickness on different locations (Sensofar S-Neox 3D Optical Profiler) on a curved lens surface with a single-layer nAR coating

- **Center: 94 nm**
- **Halfway: 108 nm**
- **Edge: 124 nm**

Figure S8. Single-layer nAR film thickness at three locations coated on a curved lens surface, with a variation within the optimal thickness range.